STRUCTURAL BIOLOGY

Structural basis for the preference of the *Arabidopsis thaliana* phosphatase RLPH2 for tyrosine-phosphorylated substrates

Anne-Marie Labandera,[1] R. Glen Uhrig,[2] Keaton Colville,[1] Greg B. Moorhead,[1]* Kenneth K. S. Ng[1]*

Despite belonging to the phosphoserine- and phosphothreonine-specific phosphoprotein phosphatase (PPP) family, *Arabidopsis thaliana Rhizobiales*-like phosphatase 2 (RLPH2) strongly prefers substrates bearing phosphorylated tyrosine residues. We solved the structures of RLPH2 crystallized in the presence or absence of sodium tungstate. These structures revealed the presence of a central domain that forms a binding site for two divalent metal ions that closely resembles that of other PPP-family enzymes. Unique structural elements from two flanking domains suggest a mechanism for the selective dephosphorylation of phosphotyrosine residues. Cocrystallization with the phosphate mimetic tungstate also suggests how positively charged residues that are highly conserved in the RLPH2 class form an additional pocket that is specific for a phosphothreonine residue located near the phosphotyrosine residue that is bound to the active site. Site-directed mutagenesis confirmed that this auxiliary recognition element facilitates the recruitment of dual-phosphorylated substrates containing a pTxpY motif.

INTRODUCTION

The control of protein function by phosphorylation is found universally across the domains of life. The protein kinases and phosphatases that catalyze the addition of phosphate groups to amino acid residues and their removal are remarkably conserved in eukaryotes and control most aspects of cell biology (*1*). Protein phosphorylation occurs predominantly on serine, threonine, and tyrosine residues, with only ~2 to 4% of the phosphorylation events in eukaryotes occurring on tyrosine residues (*2*). Most of the enzymes that dephosphorylate phosphotyrosine belong to the protein tyrosine phosphatase (PTP) family of enzymes, which contain a characteristic CX_5R catalytic motif and have a catalytic mechanism and protein fold that are distinct from those of phosphoprotein phosphatase (PPP) family enzymes, which dephosphorylate phosphoserine and phosphothreonine (*3*–*5*). Whereas the "classic" PTPs in mammals specifically target phosphotyrosine residues, other PTPs have evolved to dephosphorylate other additional cellular substrates, such as glycogen, starch, RNA, and phosphoinositides (*3*, *5*). Although plants contain a large number of tyrosine-phosphorylated proteins, only a single plant PTP enzyme has been identified compared to 38 PTPs in humans (*6*, *7*).

We have catalogued and begun to explore the evolution of protein phosphatases in plants (*6*, *8*). This work uncovered a group of predicted phosphoserine and phosphothreonine phosphatases that share sequence homology to the PPP family of mammalian enzymes, such as PP1 and PP2A. These enzymes were named after the bacterial proteins with which they share the greatest sequence similarity: the *Shewanella*-like phosphatase (SLP); the *Rhizobiales*-, *Rhodobacterales*-, and *Rhodospirillaceae*-like phosphatase (RLPH); and the ApaH-like phosphatase (ALPH) (*6*, *9*). The RLPH2 enzymes have very few eukaryotic representatives outside of photosynthetic organisms and were predicted to localize to the cytosol and nucleus. We characterized *Arabidopsis thaliana* RLPH2 (AtRLPH2) biochemically, confirmed its cytosolic localization, and unexpectedly found that it is a phosphotyrosine-specific, rather than a phosphoserine- or phosphothreonine-specific, protein phosphatase (*10*). Although the amino acid sequence of RLPH2 contains key motifs shared with phosphoserine- and phosphothreonine-specific phosphatases in the PPP family, RLPH2 has several unique properties, including not only being resistant to the classic serine-threonine phosphatase inhibitors okadaic acid and microcystin but also being sensitive to the PTP phosphatase inhibitor vanadate. RLPH2 is the only known example of a eukaryotic PPP-family phosphatase that strongly prefers to dephosphorylate tyrosine-phosphorylated substrates. To better understand the structural basis underlying these properties, we determined the structure of AtRLPH2 by x-ray crystallography and confirmed key structure-function relationships using site-directed mutagenesis, revealing several structural features that explain the unique adaptations found in the RLPH class of protein phosphatases.

RESULTS

Overall structure of AtRLPH2

We determined the three-dimensional structure of AtRLPH2 by single-wavelength anomalous diffraction (SAD) phasing using the anomalous scattering at a wavelength of 1.853 Å from the sulfur atoms and divalent metal cations in the native protein. About two-thirds of the structure was built automatically using the initial map extending to a resolution limit of 2.2 Å. The remaining portion of the structure was gradually built by combining phases calculated from the SAD data with phases calculated from the model, as well as through further refinement of the model against data extending to a resolution limit of 2.0 Å from a second native crystal (data collection and refinement statistics in Table 1). Further refinement of the structure, including the active site, was completed using a crystal grown in the presence of the phosphate mimic sodium tungstate to identify phosphate-binding sites. The structures refined against the three different data sets are isomorphous, with only slight differences between the native and tungstate complex structures near the divalent metal cations at the active site. At the conclusion of refinement, only residues 1 to 3 and 140 to 147 were not clearly defined by electron density maps.

[1]Department of Biological Sciences, University of Calgary, 2500 University Drive Northwest, Calgary, Alberta T2N 1N4, Canada. [2]Department of Biological Sciences, University of Alberta, Edmonton, Alberta T6G 2R3, Canada.
*Corresponding author. Email: moorhead@ucalgary.ca (G.B.M.); ngk@ucalgary.ca (K.K.S.N.)

Table 1. Crystallographic statistics.

Crystal	Native I	Native II	Sodium tungstate
PDB code		5VJV	5VJW
Unit cell dimensions $a = b$, c (Å)	102.23, 60.75	102.60, 61.04	102.66, 60.21
Wavelength (Å)	1.8532	1.03318	1.21416
Resolution (Å)*	40–2.20 (2.26–2.20)	40–1.95 (2.00–1.95)	40–1.80(1.85–1.80)
R_{sym}†	0.092 (0.405)	0.109 (1.15)	0.098 (0.95)
CC1/2‡	1.000 (0.975)	0.998 (0.537)	0.998 (0.641)
$I/\sigma I$	35.3 (8.9)	12.1 (1.6)	12.3 (1.9)
Completeness (%)	93.1 (75.2)	99.5 (98.7)	99.0 (99.0)
Redundancy	30.9 (27.1)	5.5 (5.5)	5.0 (5.0)
Refinement			
Resolution (Å)		40–1.95	40–1.80
Unique reflections		25,380	31,880
R_{work}§/R_{free}¶		0.184/0.219	0.176/0.199
Total number of atoms		2,555	2,561
Protein atoms		2,343	2,343
Phosphate/tungstate atoms		4	8
Water atoms		208	210
Average B-factors (protein)		26.4	20.5
Average B-factors (water)		34.1	29.0
Average B-factors (metal ions)		23.1	16.5
Average B-factors (phosphate/tungstate ions)		32.2	35.3
RMSD from ideal geometry			
Bond lengths (Å)		0.008	0.007
Bond angles (°)		1.20	1.20
Ramachandran outliers‖		0	0
Ramachandran favored‖ (%)		96.6	96.6
Clash score**		0.86	0.43
MolProbity score (percentile)‖		0.98 (100)	0.87 (100)

*Values from the outermost resolution shell are given in parentheses. †$R_{sym} = \Sigma_i |I_i - \langle I \rangle| / \Sigma_i I_i$, where I_i is the ith integrated intensity of a given reflection and $\langle I \rangle$ is the weighted mean of all measurements of I. ‡Percentage of correlation between intensities from random half–data sets (*33*). §$R_{work} = \Sigma||F_o| - |F_c|| / \Sigma|F_o|$ for 95% of reflection data used in refinement. ¶$R_{free} = \Sigma||F_o| - |F_c|| / \Sigma|F_o|$ for 5% of reflection data excluded from refinement. ‖Ramachandran plot analysis performed in MolProbity (*34*). **Number of serious steric overlaps (>0.4 Å) per 1000 atoms.

The three-dimensional structure of AtRLPH2 reveals three distinct structural domains arranged around a central pair of divalent metal ions in the active site. One of the metal ions is coordinated to protein side chains located in loops that project from a central mixed β-sandwich of domain 1; the other metal ion is coordinated by side chains from residues in domain 2 and in the loop connecting domains 2 and 3 (Figs. 1 and 2A). Domain 1 is made of noncontiguous residues (1 to 78, 190 to 212, and 258 to 309), domain 2 of residues 79 to 189, and domain 3 of residues 213 to 257. Looking directly into the active site, the N terminus of the protein is located just below the central β-strand (β1) in the five-stranded β-sheet of the β-sandwich (Fig. 1). The loop following β1 contains two of the amino acid residues (Asp^{13} and His^{15}) that coordinate divalent metal ion 1 at the active site (Fig. 2A). These residues, as well as others described below, are conserved in various RLPH proteins (fig. S1). This loop is followed by α-helices α1 and α2, which pack against the β-sandwich, and β2, which pairs with β1. The loop following β2 contains Asp^{47}, the only residue participating in the coordination of both divalent metal ions 1 and 2, and Arg^{51}, which is poised to interact with the phosphoryl group in the substrate before hydrolysis. The next structural element in the sequence is the α-helix α3, which connects to β3 at the back of sheet 1, thus completing the first half of domain 1.

The loop following β3 leads into the first part of domain 2. Domain 2 starts with a central α-helix (α4) in which the N-terminal residue Asn^{80} coordinates to divalent metal ion 2 at the active site (Fig. 2A). The positively charged end of the macrodipole of this central α-helix points toward the negatively charged phosphoryl groups of the substrate. A series of six loops and six α-helices follow α4 to form the

"top" of domain 2 of the protein (residues 80 to 188). Residues 140 to 147 in a long loop in the middle of this domain are disordered and located adjacent to the peptide-binding groove (movie S1). Notably, the side chain of Tyr^{149} is near the boundary of the disordered region of this loop and is predicted to be located within 4 to 5 Å of the bound peptide.

Immediately following the end of domain 2 are three β-strands (β4 to β6), two of which form an antiparallel hairpin that pairs with the rest of β-sheet 2, which is formed by the C-terminal portion of the protein. The loop following β6 contains His^{213}, the side chain of which coordinates to metal ion 2. Residues 214 to 260 form a small domain (domain 3) with two short α-helices (α11 and α12) and primarily irregular secondary structure that is unique to AtRLPH2 and closely related homologs. The guanidino group of Arg^{245} in domain 3 forms the other side of a clamp around the phosphoryl group of the substrate, in which the guanidino group of Arg^{51} forms the other side of the clamp. Immediately following domain 3 is β7, the first strand in the final portion (domain 1c) of domain 1. β7 contains the previously identified version of motif 1 that is unique to RLPH2 (Fig. 1 and figs. S1 and S2) (*8*) and pairs with β6 in β-sheet 2 of domain 1. His^{266} (the penultimate residue of motif 1) is found in the loop that follows and is the most C-terminal residue that participates in coordinating to the divalent metal ions. This long loop leads into a series of four β-strands (β8 to β11), which complete β-sheet 1 and in which β11 pairs in an antiparallel arrangement with β1, all part of structural domain 1. A short segment of nonregular secondary structure follows the end of β11 to form the C terminus of the protein.

In summary, the β-sandwich at the heart of domain 1 provides a platform from which five key loops protrude into the central active-site cleft to coordinate to two divalent metal cations and to form half of the substrate-binding channel (Fig. 2 and movie S1). All of these key residues are conserved in the active sites of other PPP-family enzymes, including mammalian PP1 (Fig. 2B). The mostly α-helical domain 2 and a small flanking domain 3 combine to form portions of the substrate-binding groove (movie S1) that appear to define substrate recognition in AtRLPH2.

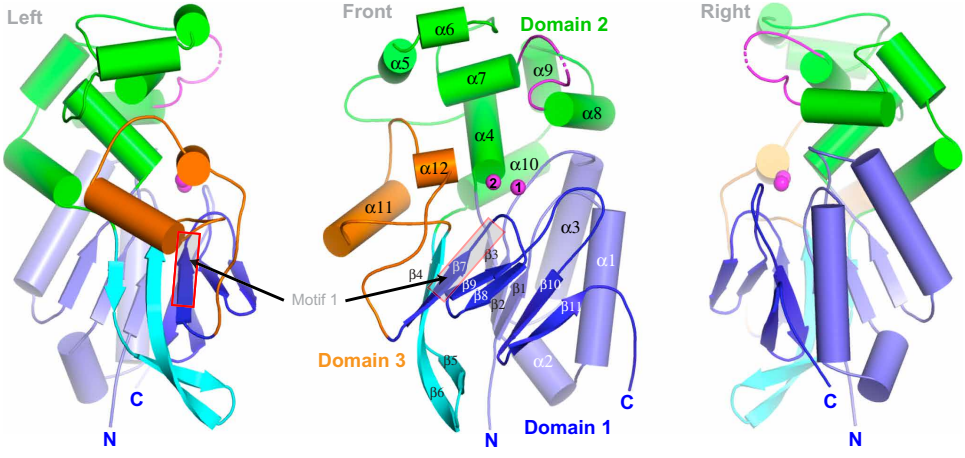

Fig. 1. Ribbon diagram showing the path of the AtRLPH2 polypeptide chain and global arrangement of secondary structure elements. Domains 1, 2, and 3 are colored blue, green, and orange, respectively. The dashed line in the loop (magenta) between α-helices 7 and 8 indicates a region of disorder not defined by clear electron density. Metal ions 1 and 2 are pink, and the position of motif 1 (residues 262 to 267, VVSGHH) is indicated with a box.

Comparisons with other phosphatase structures

The central β-sandwich domain 1 in AtRLPH2 corresponds to a highly conserved structural element characteristic of the members of the PPP family (*11*), as well as the slightly more closely related cold-active PTPs (CAPTPs) (*12*), diadenosine tetraphosphatases (*13*), and polynucleotide phosphatases (Fig. 3, A to D) (*14*, *15*). We compared this element of the three-dimensional structure of AtRLPH2

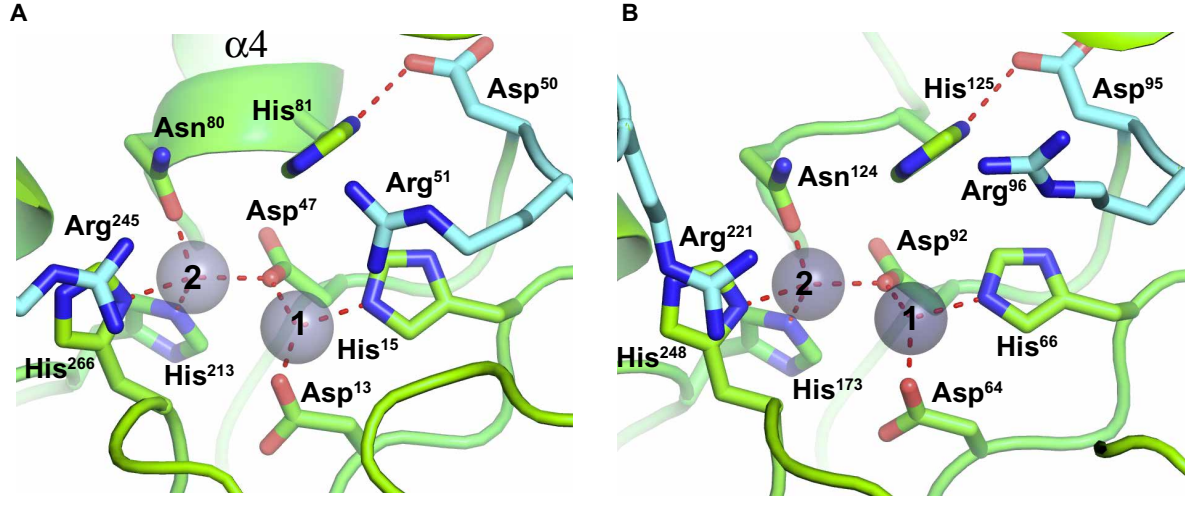

Fig. 2. Coordination of divalent metal ions in the active sites. Metal ions 1 and 2 are coordinated in the active sites of (**A**) AtRLPH2 and (**B**) rabbit PP1 [Protein Data Bank (PDB) code 1FJM] as shown. Ions are colored gray, and coordination bonds are shown as red dashed lines. Highly conserved residues that are important for metal ion coordination, substrate recognition, or catalysis are shown as stick representations and labeled.

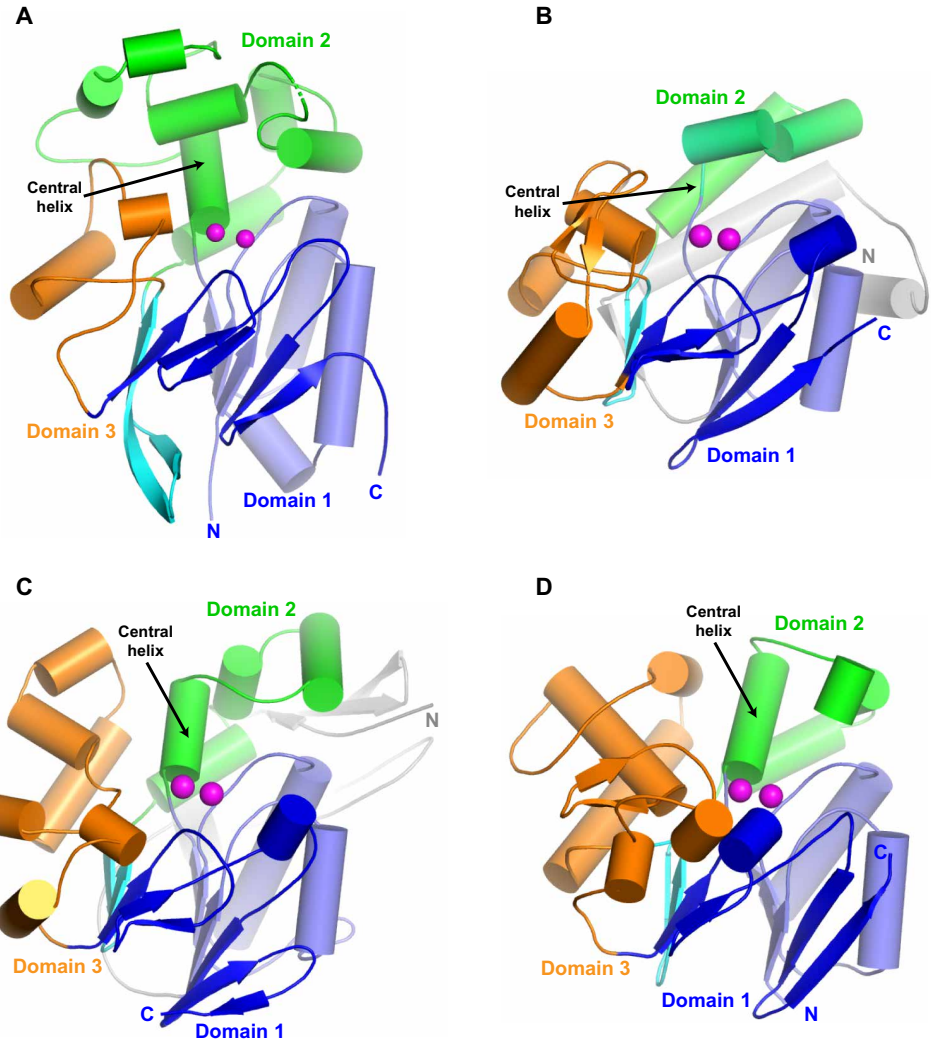

Fig. 3. Comparison of the three-dimensional structures of PPP-family phosphatases. Domain 1 shown in the same orientation in (**A**) AtRLPH2, (**B**) rabbit PP1 (PDB code 1FJM), (**C**) *Shewanella* CAPTP (PDB code 1V73), and (**D**) *Shigella* diadenosine tetraphosphatase (PDB code 2DFJ). Domain 1, blue; domain 2, green; domain 3, orange; metal ions, pink.

with those in previously determined three-dimensional structures of related proteins using the distance alignment matrix method (DALI) algorithm (*16*). The closest relatives of AtRLPH2 all share with it the β-sandwich domain and central α-helix (α4 at the start of domain 2), with the highest amount of similarity seen for the CAPTP from *Shewanella* sp. [1V73, 2Z72, z = 18.9, root mean square deviation (RMSD) = 2.9 Å, n = 205 residues], the diadenosine tetraphosphatases from *Shigella flexneri* 2a (2DFJ, z = 19.6, RMSD = 2.7 Å, n = 210 residues) and *Trypanosoma brucei* (2QJC, z = 19.0, RMSD = 2.4 Å, n = 181 residues), the polynucleotide phosphatase from *Clostridium thermocellum* (4J6O, z = 18.8, RMSD = 2.7 Å, n = 199 residues), and the bacteriophage λ-phosphatase (1G5B, z = 17.0, RMSD = 3.2 Å, n = 192 residues). The catalytic subunits from members of the PPP family also contain the central β-sandwich domain but lack the central α-helix, resulting in slightly lower structural alignment scores for RLPH2 with PP2B (5C1V, z = 16.0, RMSD = 3.3 Å, n = 202 residues), PP5 (3H62, z = 15.9, RMSD = 3.2 Å, n = 202 residues), PP2A (4I5L, z = 15.8, RMSD = 3.4 Å, n = 203 residues), and PP1 (4MOV, z = 15.7, RMSD = 3.2 Å, n = 199 residues).

Related to these global structural similarities, the coordination of metal ions at the active site of AtRLPH2 is perfectly conserved when compared to the CAPTPs, diadenosine tetraphosphatases, polynucleotide phosphatases, and PPPs (Figs. 2 and 3). With respect to the region immediately adjacent to the divalent metal cation coordination sphere, the most distinctive difference between the serine- and threonine-specific PPPs and these other phosphatases, including AtRLPH2, is the lack of the central α4 helix in the PPPs (Figs. 1 and 3). Despite this difference, however, the side chain of the first residue in this helix (Asn^{80}) that coordinates to metal ion 2 is perfectly conserved, as is the imidazole side chain of the following His^{81} residue, which does not directly coordinate to the metal ions but likely donates a hydrogen bond to the phosphorylated substrate (Fig. 2 and figs. S1 and S2). The proximity of the negatively charged carboxylate side chain of the highly conserved Asp^{50} residue (Fig. 2), which is equivalent to Asp^{117} in CAPTP and Asp^{95} in rabbit PP1, is expected to stabilize the protonated form of His^{81}, thus raising its pK_a (where K_a is the acid dissociation constant) and making it possible for the residue to act as a general acid catalyst, donating a proton to stabilize and promote the formation of the phosphate leaving group (*17*).

The most distinctive parts of the tertiary structure of AtRLPH2 are found in domains 2 and 3. Apart from the central α4 helix, which appears to be shared with CAPTP, the diadenosine tetraphosphatases, and polynucleotide phosphatases, the structure of domain 2 appears to be unique to AtRLPH2. In place of domain 2, the serine- and threonine-specific PPPs have three α-helices, the second of which occupies a position in the substrate-binding cleft somewhat similar to that of α8 of AtRLPH2, but the rest of domain 2 is absent (Fig. 3). Aside from the central α4 helix, which is shared with CAPTP, the diadenosine tetraphosphatases, and polynucleotide phosphatases, the remainder of the structure of AtRLPH2 domain 2 and the structure of AtRLPH2 domain 3 also differ from the equivalent regions of enzymes from the PPP family and the other more closely related phosphatases. The unique structures of domains 2 and 3 and the positioning of these two domains adjacent to the active-site cleft suggest that these two domains may be key determinants of substrate recognition characteristic of the RLPH class of enzymes. In support of this notion are the structures of the PP1/MYPT (*18*), PP1/spinophilin (*19*), and PP2A (*20*, *21*) holoenzyme complexes, in which accessory (regulatory) subunits contribute structural elements adjacent to the divalent metal ions bound to the catalytic subunit.

These structural elements are presumably important for determining the binding specificity of the holoenzyme and are located in the same region relative to the active site as that occupied by AtRLPH2 domain 2.

Recognition of tyrosine-phosphorylated and dual threonine- and tyrosine-phosphorylated substrates

Although the coordination of two divalent metal ions at the active site and the structure of the β-sandwich domain closely resemble the analogous features of PPP family members and other related phosphatases, these features only define a portion of the active-site cleft that is used for substrate recognition. As mentioned above, some of the unique structural features of domains 2 and 3 likely help to define the binding specificity for the phosphoprotein substrates of AtRLPH2.

Our previous work demonstrated that AtRLPH2 displays a clear preference for substrates containing phosphotyrosine compared to substrates containing phosphoserine or phosphothreonine (*10*). Upon exploring additional peptides as substrates, we discovered that AtRLPH2 readily dephosphorylated peptides derived from mammalian mitogen-activated protein kinases (MAPKs) within their dual phosphorylated pTxpY activation loops and these were some of the best substrate peptides we identified. To explore this further, we monitored dephosphorylation of a mammalian extracellular signal–regulated kinase 1 and 2 (ERK1/2) activation loop peptide phosphorylated either solely on the tyrosine (pY) or on both the threonine and tyrosine residues (pTEpY) (Fig. 4A). AtRLPH2 showed little to no activity against the threonine-only phosphorylated peptide (pTEY) (fig. S3). Although the enzyme displayed substantial activity against the ERK1/2 peptide phosphorylated solely on tyrosine (TEpY), phosphorylation at both threonine and tyrosine (pTEpY) substantially increased V_{max}/K_m (Fig. 4A) and reduced the K_m eightfold, from 1.44 to 0.18 mM. V_{max} was about the same for both peptides, although it should be noted that V_{max} and K_m were not precisely determined for the TEpY peptide because of the modest solubility of the peptide substrate. These results suggest that AtRLPH2 may dephosphorylate both residues or that the phosphothreonine might promote dephosphorylation of the phosphotyrosine. To distinguish between these two possibilities, we spotted the phosphopeptides on a membrane, incubated the membrane with AtRLPH2, and then probed the membranes with antibodies specific to phosphotyrosine or phosphothreonine (Fig. 4, B to E). AtRLPH2 displayed little activity toward the phosphothreonine site in either the TEpY or pTEpY peptide, but the presence of the phosphothreonine N-terminal to the phosphotyrosine enhanced its activity toward the phosphotyrosine site, similar to the enhanced activity observed in Fig. 4A when using the dual-phosphorylated peptide. This substrate preference suggests that a secondary binding site for phosphothreonine may be located near the active site that aids in substrate recruitment for dual-phosphorylated substrates, decreasing K_m and thus increasing V_{max}/K_m.

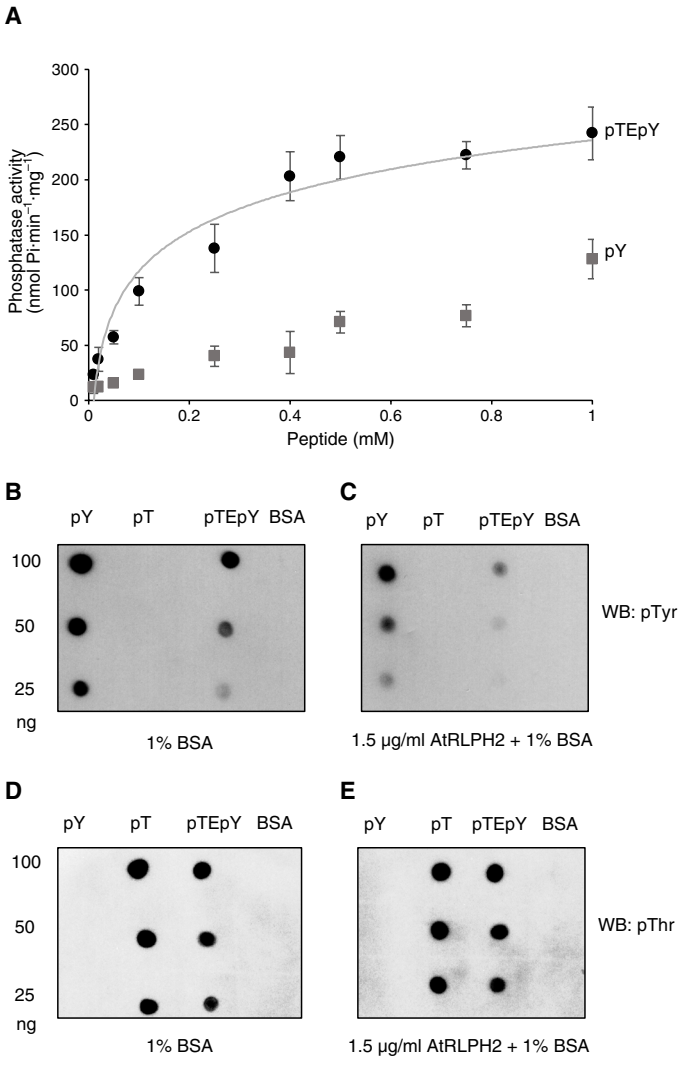

Fig. 4. AtRLPH2 preferentially dephosphorylates phosphotyrosine substrates that contain an N-terminal phosphothreonine. (**A**) Kinetic analysis of dephosphorylation of various concentrations of extracellular signal–regulated kinase 1 and 2 (ERK1/2) phosphopeptides by recombinant AtRLPH2. Assays were performed using ERK1/2 phosphopeptides HTGFLTEpYVATR (TEpY, squares) and HTGFLpTEpYVATR (pTEpY, circles), and kinetic analysis was used to determine V_{max} and K_m. V_{max} was about the same for both peptides (~240 nmol min^{-1} mg^{-1}). K_m for peptide HTGFLTEpYVATR was 1.44 mM, and K_m for HTGFLpTEpYVATR was 0.18 mM. Error bars represent ±SE ($n = 3$). (**B** to **E**) On-blot dephosphorylation assays. Singly phosphorylated (TEpY and pTEY) and dually phosphorylated (pTEpY) ERK1/2 phosphopeptides covalently coupled to bovine serum albumin (BSA) were spotted onto a nitrocellulose membrane and incubated with either BSA alone (B and D) or BSA plus recombinant AtRLPH2 (C and E). Final phosphorylation status was assessed by Western blot (WB) with an antibody specific for phosphotyrosine (B and C) or phosphothreonine (D and E). All blots were performed three times in parallel and developed at the same time, and one representative blot is shown.

Structural determinants of substrate recognition

Consistent with the preference for dual-phosphorylated substrates is the observation of tungstate ions in the structure of AtRLPH2 that was cocrystallized with 1 mM sodium tungstate, a well-studied mimic of phosphate in phosphoryl transfer reactions (*17*, *22*). The strong and anomalous scattering of the tungsten atom in tungstate provides definitive evidence localizing two tungstate ions near the active site (Fig. 5A). Tungstate ion 1 forms coordination bonds with the two divalent metal ions in the same manner, as seen previously in PP1 (*17*). In the native structure of AtRLPH2, a phosphate ion appears to be bound in the same position, something not seen previously in either PP1 or other PPP-family enzymes. Notably, phosphate was not added during either purification or crystallization, indicating a fairly high affinity for phosphate. A second tungstate ion forms hydrogen

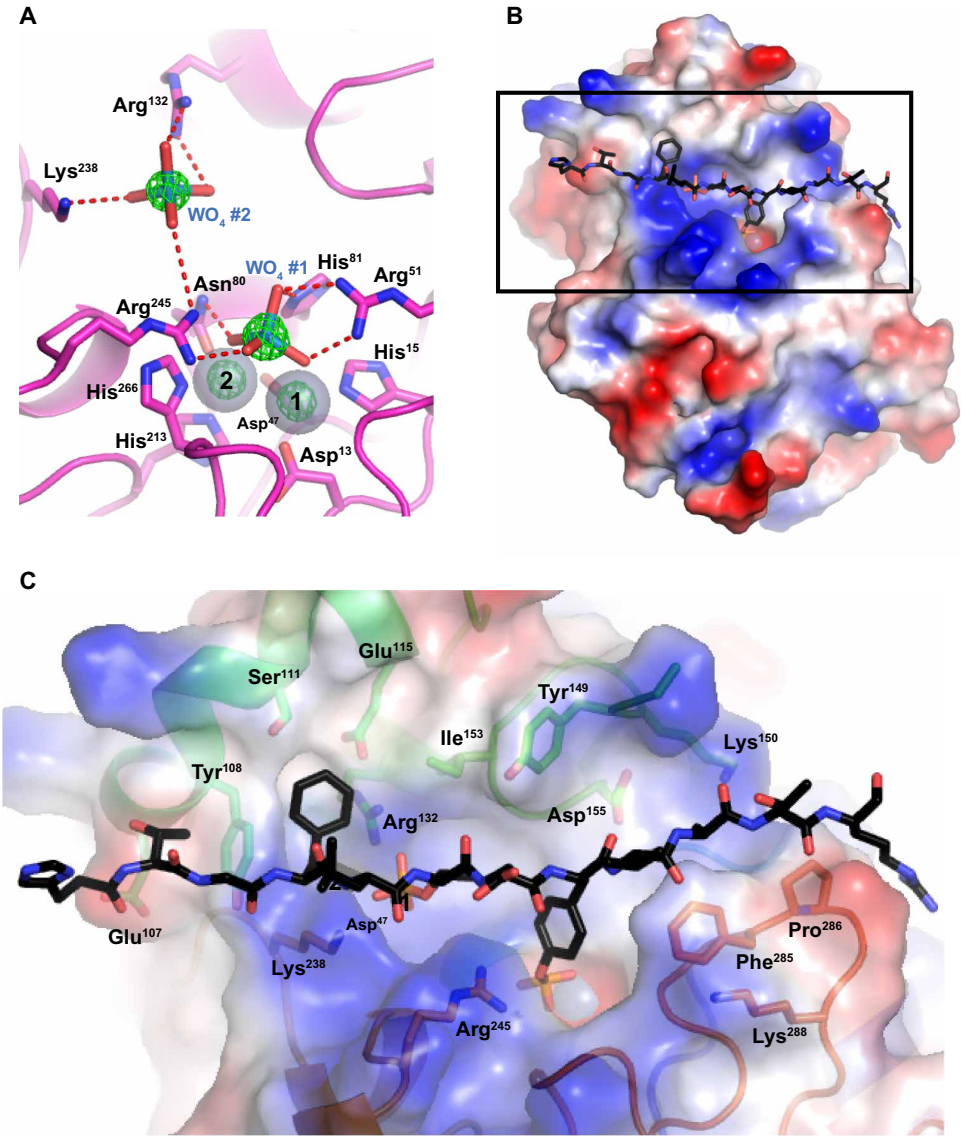

Fig. 5. Coordination of tungstate ions and model of a substrate peptide bound to AtRLPH2. (**A**) Hydrogen-bonding interactions between tungstate (red bars) and amino acid side chains are indicated by red dashed lines. The anomalous difference electron density map is shown as a green mesh (contoured at 10 SDs). (**B**) The structure of AtRLPH2 is shown as a solvent-accessible surface representation colored according to electrostatic potential, with blue indicating positive potential, white indicating neutral potential, and red indicating negative potential. The peptide HTGFLpTEpYVATR was modeled into the substrate. (**C**) Higher-magnification view of the boxed area in (B). The peptide substrate was modeled with the phosphoryl group of the phosphothreonine residue positioned in the same place as the tungstate ion seen in the complex of AtRLPH2 cocrystallized with tungstate and the phosphoryl group of the phosphotyrosine residue positioned next to the divalent metal cations, also coincident with a bound tungstate ion in the tungstate cocrystal structure. Semitransparent surface representation shown over ribbon diagram and stick representation of the crystal structure.

bonds and electrostatic interactions with the positively charged side chains of Arg^{132} and Lys^{238}, and is about 4 Å from Arg^{245}. Arg^{132} and Lys^{238} are located in domains 2 and 3, respectively, regions of the structure of AtRLPH2 that are unique to RLPH2 class of enzymes (Fig. 5A). Consistent with their putative role in recognizing a secondary phosphoryl group in the substrate, all three of these residues are highly conserved in the diverse members of the RLPH2 class (fig. S1), but are not conserved in other PPP family members (fig. S2).

Models of peptides adopting an extended polypeptide backbone conformation indicate that peptides with a pTxpY sequence can bind in a manner wherein the phosphoryl group of the phosphotyrosine is coordinated to the divalent metal ions and a bound water molecule at the same location as tungstate ion 1 in the active site (Figs. 5, B and C, and 6, A and B). This model also predicts that the phosphoryl group of phosphothreonine is located at the same position as that seen for tungstate ion 2, forming stabilizing interactions with the side-chain amino and guanidino groups of Lys^{238} and Arg^{132}, respectively.

To confirm the recognition of phosphothreonine by Lys^{238} and Arg^{132}, we converted these residues to Ser by site-directed mutagenesis. The R132S mutant and the R132S, K238S double mutant displayed weak activity against the pTEpY peptide (~2 to 5% of wild-type activity), indicating the particular importance of Arg^{132} for the recognition of a phosphothreonine two positions N-terminal to the phosphotyrosine residue (fig. S3A). In comparison, both of these mutants showed only an approximate 50% reduction in activity for the recognition of the same peptide lacking the phosphoryl group on the threonine residue (TEpY peptide, fig. S3A). In contrast, the slight reduction in activity for the pTEpY peptide and dramatic increase in activity for the TEpY peptide seen for the K238S mutant indicate a very different, auxiliary role for substrate recognition. The more peripheral location of Lys^{238} near the position predicted for the phosphoryl group of a peptide containing phosphothreonine is consistent with the moderate reduction in activity of the K238S form of AtRLPH2 for the pTEpY peptide substrate compared to that of wild-type AtRLPH2 (fig. S3A). More interesting was the large increase in activity for the TEpY peptide lacking the secondary phosphoryl group. Modeling of the structure of this peptide suggested that the lack of the secondary phosphoryl group would allow the side chain of the threonine residue to adopt a different rotamer in which the side-chain hydroxyl group would be able to form hydrogen-bonding interactions with both the side-chain guanidino group of Arg^{132} and the side-chain hydroxyl group of Tyr^{149} (fig. S4, A and B). Coupled with the loss of the favorable phosphoryl group interaction with Arg^{132} and Lys^{238}, together, this may account for the low activity of the TEpY peptide

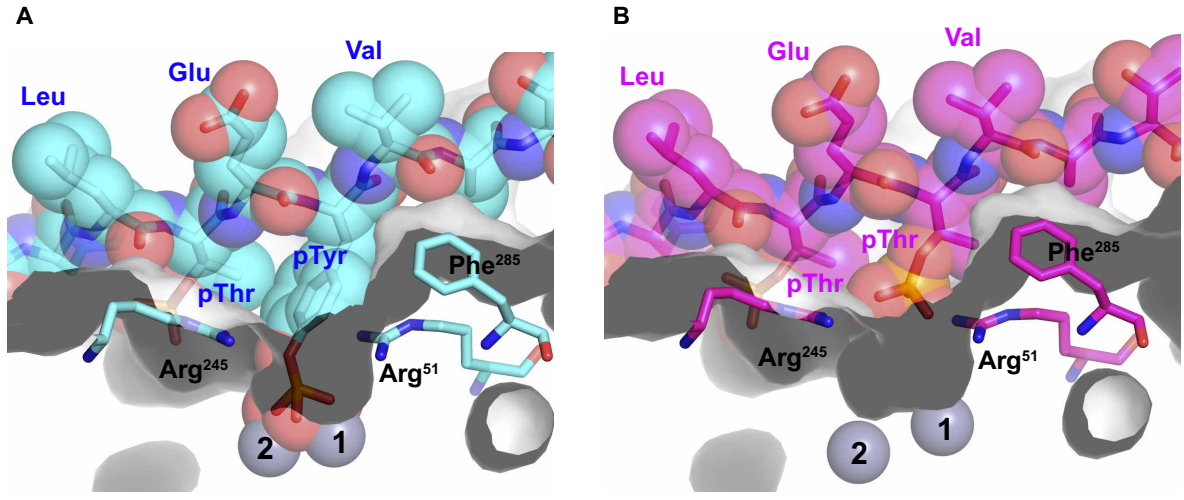

Fig. 6. A double-arginine gating mechanism contributes to the substrate specificity preference for phosphotyrosine. (**A**) Stick and semitransparent surface model of AtRLPH2 (gray) bound to an ERK1/2 peptide (blue) with the peptide's phosphotyrosine bound to the divalent metal ions coordinated in the active site of AtRLPH2. (**B**) Model of AtRLPH2 bound to an ERK1/2 peptide in which the peptide's phosphotyrosine residue is replaced with phosphothreonine (pink). The arrangement of AtRLPH2 Arg^{51}, Arg^{245}, and Phe^{285} creates a binding pocket that allows the longer side chain and flat aromatic ring to extend the phosphoryl group of the phosphotyrosine residue toward the divalent metal ions (A). The shorter phosphothreonine residue does not allow the phosphoryl group to reach deep enough into the pocket to reach the divalent metal ions (B).

when Lys^{238} is present, as in the wild-type enzyme and in the R132S mutant, when compared with the greatly increased activity when Lys^{238} is replaced with a much shorter serine side chain in the K238S mutant (fig. S4, A and B). This interpretation is supported by activity assays with the R132S, K238S double mutant (fig. S3A). Given that both Arg^{132} and Lys^{238} are highly conserved in the RLPH class, our structural and mutagenesis results strongly suggest that these two residues work in concert in all members of the RLPH class to provide a selective positive filter for a nearby phosphothreonine residue and a selective negative filter for a nearby threonine residue.

Close inspection of the model of AtRLPH2 bound to the dually phosphorylated ERK1/2 peptide also suggests a mechanism accounting for the observed preference for the dephosphorylation of phosphotyrosine over that of phosphothreonine or phosphoserine (Fig. 6, A and B). The side-chain guanidino groups of Arg^{245} and Arg^{51} converge on the binding pocket for the phosphoryl group bound to the divalent metal cations. In addition, the phenyl group side chain of Phe^{285} is packed against the side chain of Arg^{51} and forms part of the binding pocket for the residue being dephosphorylated and the residue immediately C-terminal to it. The residues from domain 3 (Arg^{245}) and domain 1c (Phe^{285}) help to create a gating mechanism that restricts the entry of shorter phosphorylated side chains that is not seen in the more open active site architecture of enzymes like PP1, which dephosphorylate substrates with phosphoserine and phosphothreonine much more efficiently than phosphotyrosine. The importance of these residues for activity is illustrated in enzymatic assays using forms of AtRLPH2 in which Arg^{51} and Arg^{245} were mutated to alanine (fig. S3B). Compared to wild-type AtRLPH2, the R51A and R245A mutant forms of AtRLPH2 exhibited highly reduced activity toward peptides phosphorylated only on Tyr (TEpY) and those phosphorylated dually on both Thr and Tyr (pTEpY) and a consistently low activity toward the peptide phosphorylated only on threonine (pTEY). Arg^{245} is conserved throughout all RLPH2 sequences, whereas the equivalent of Phe^{285} is always a large hydrophobic amino acid such as phenylalanine or tyrosine (fig. S1). Other residues, such as Tyr^{108}, Ile^{153}, and Asp^{155}, which are also highly conserved and line the putative substrate-binding groove of AtRLPH2, also likely help to position the peptide segment around the phosphotyrosine residue in a manner that further enhances the substrate specificity for the pTXpY motif (Fig. 5C and movie S1).

We previously noted the unique and remarkably conserved region in RLPH enzymes that we designated motif 1 (figs. S1, S2, and S5, A and B) (*8*). The crystal structure of AtRLPH2 indicates that motif 1 occupies a central position at the first β-strand (β7) following the end of domain 3 and the beginning of domain 1c. This motif mediates interactions between domain 3 and domain 1, helping to position one of the ligands for divalent metal ion 1 (His^{266}, the second-to-last residue of motif 1), as well as Arg^{245}, one of the gatekeeper residues in domain 3, which also packs against the two last residues (His^{266} and His^{267}) in motif 1 (fig. S5). The high sequence conservation of motif 1 in members of the RLPH2 class and variance in this motif in other PPP-family enzymes both suggest a key role for the interface between domains 1 and 3, as well as the gatekeeper Arg^{245} residue, in defining the substrate specificity of RLPH2 enzymes.

DISCUSSION

The substrate specificity of the RLPH2 enzyme from *Arabidopsis* was previously defined through a biochemical approach and found to be highly specific for phosphotyrosine, although the sequence of the enzyme revealed a catalytic core that is characteristic of the PPP family (*8*, *10*). In addition, AtRLPH2 was found to be sensitive to the tyrosine phosphatase inhibitor vanadate, which typically does not affect the activities of PPP enzymes. The identification and characterization of this tyrosine phosphatase in plants are particularly relevant because, although the amount of protein tyrosine phosphorylation is similar to that found in humans (*8*, *23*, *24*), only a small number of bona fide classic tyrosine phosphatases and kinases have been identified in plants through genome sequencing and biochemical approaches (*7*). This suggests that noncanonical tyrosine-specific phosphatases

and kinases likely play important roles in regulating tyrosine-specific phosphorylation signaling events in plants. The present work provides structural and mechanistic insights into the unique functional properties of an atypical tyrosine-specific protein phosphatase in plants, revealing how modifications to the structure of a PPP-family enzyme can generate specificity for the dephosphorylation of a pTXpY sequence, a motif commonly found in MAPK activation loops (*25*).

The coordination of divalent metal ions at RLPH2's active site is remarkably conserved when compared to other serine- and threonine-specific PPP-family protein phosphatases. The residues residing in the active site coordinate to divalent metal ions (likely Fe^{2+} and Mn^{2+}), which in turn directly coordinate to the phosphoryl group of the substrate. The strong similarity of the structure of the AtRLPH2 active site to that of other PPP enzymes suggests a direct metal-dependent dephosphorylation mechanism that differs from the mechanism seen in classic PTP enzymes (*3*, *17*, *26*).

Despite the many similarities of the AtRLPH2 active site to that of PP1 and other PPP enzymes, several key differences appear to account for the enzyme's unusual preference for phosphotyrosine, in contrast to the preference for phosphoserine and phosphothreonine seen in most PPP enzymes. The crystal structure of AtRLPH2 shows that similarities with PPP enzymes are restricted to domain 1, which contributes most of the side-chain ligands coordinating to the perfectly conserved divalent metal ions at the heart of the active site, and forming a platform for half of the substrate-binding active site channel. However, the structures of the two other domains, which also contribute determinants of substrate specificity, share very few similarities with domains 2 and 3 from other PPP enzymes (Fig. 3). The single most important determinant of specificity for phosphotyrosine appears to be the gatekeeper function of the terminal guanidino groups of Arg^{51} and Arg^{245} (Figs. 5 and 6). Whereas Arg^{51} is a highly conserved residue from domain 1 that is also found in most other PPP enzymes, Arg^{245} is found in domain 3, which has a very different structure in other PPP enzymes, apart from homologs in the RLPH2 class. Despite fundamental differences in the structure of domain 3, the guanidino group of Arg^{221} in human PP1 and Arg residues in other related enzymes like CAPTP, the diadenosine tetraphosphatases, and polynucleotide phosphatases are located in nearby but nonidentical positions to that occupied by Arg^{245} (fig. S2). It is noteworthy that CAPTP can also dephosphorylate substrates bearing phosphotyrosine, but has not been shown to dephosphorylate substrates bearing phosphoserine or phosphothreonine (*27*). We thus propose that some of these differences in the structure of domain 3 affect the position of the guanidino group of this arginine residue in a way that affects the accessibility of phosphotyrosine versus phosphothreonine and phosphoserine. In addition, the structure of domains 2 and 3 in AtRLPH2 positions several other residues that are only conserved in the RLPH class. The bulky aromatic side chains of Tyr^{108}, Tyr^{149}, and Phe^{285}, as well as the side chains of Ile^{153} and Asp^{155}, all combine to define the shape of the substrate-binding cleft of AtRLPH2 in a way that likely helps to present the phosphotyrosine residue of the substrate in a manner favorable for binding and catalysis (Figs. 5 and 6 and movie S1). Structural elements like motif 1 in domain 1c also likely play a role in forming a brace that positions structural elements in domains 2 and 3. In combination with the gatekeeper functions of the Arg^{51} and Arg^{245} residues immediately adjacent to the divalent metal ions, these features of AtRLPH2 appear to combine to create a distinctive specificity for phosphotyrosine.

Another distinctive feature of AtRLPH2 is the preference for dual-phosphorylated substrates with a pTXpY motif. The crystal structure reveals the presence of a shallow pocket lined by the positively charged side chains of three highly conserved basic residues (Arg^{132}, Lys^{238}, and Arg^{245}) from domains 2 and 3 that are located near the divalent metal cations at the active site (Fig. 5, B and C). Tungstate is a widely used mimic of phosphate, and its strong anomalous scattering signal identified two ions when AtRLPH2 was cocrystallized in the presence of tungstate (*17*, *28*). One ion coordinates directly with both divalent metal ions in the active site, mimicking the phosphoryl group of the substrate. The second ion forms favorable electrostatic interactions with Arg^{132} and Lys^{238}, apparently mimicking the phosphoryl group from a phosphothreonine residue located two positions N-terminal to the phosphotyrosine residue coordinated to the divalent metal ions at the active site. The model of the dual-phosphorylated ERK1/2 peptide with extended backbone conformation bound to the enzyme active site reveals perfect alignment of the two phosphoryl groups with the positions observed for the tungstate ions. This model also shows the presence of stabilizing packing interactions between the side-chain methyl group of the phosphothreonine residue and the aromatic ring of the phosphotyrosine residue, possibly accounting for the enzyme's preference for phosphothreonine over phosphoserine through this auxiliary recognition element (Figs. 5 and 6).

These structural observations are consistent with in vitro studies of substrate specificity using phosphorylated peptides. On-blot and solution-phase dephosphorylation assays show that AtRLPH2 preferentially dephosphorylates phosphotyrosine when phosphothreonine is also present in the substrate. Moreover, when two of the residues in the phosphothreonine-binding pocket (Arg^{132} and Lys^{238}) are mutated to serine, the preference for substrates with a pTXpY motif over substrates with TXpY disappears. This suggests that the endogenous AtRLPH2 substrate likely has another phosphorylated residue two amino acids N-terminal of the phosphotyrosine. MAPKs are dually phosphorylated on a TXY motif to be activated (*25*, *29*). In accordance with the information provided by the structure and dephosphorylation assays, it is reasonable to propose that plant MAPKs may be substrates for AtRLPH2.

Our analysis of structure-function relationships in AtRLPH2 provides a molecular basis for further exploring the physiological roles of a poorly characterized class of atypical PTPs. Our results suggest that in addition to dual-phosphorylated, activated MAPKs, the endogenous substrates of AtRLPH2 and other enzymes in the RLPH class may include other dual-phosphorylated proteins bearing the pTXpY motif. Further research using phosphoproteomic and genetic approaches are needed to identify and validate the full range of substrates and physiological roles of enzymes in the RLPH class.

MATERIALS AND METHODS

Protein expression and purification

AtRLPH2 was expressed as reported by Uhrig *et al.* (*10*). Cells were stored frozen and thawed in resuspension buffer [50 mM Hepes-NaOH (pH 7.5), 150 mM NaCl, 5% (v/v) glycerol, 10 mM imidazole, 1 mM benzamidine, and 1 mM phenylmethylsulfonyl fluoride] before lysis using a French press (three rounds at 1000 psi). After centrifugation at 50,000*g* for 35 min, the supernatant was filtered through Miracloth and loaded onto a 1-ml HisTrap HP column (GE Healthcare) at 1 ml/min. The column was washed with buffer

A [50 mM Hepes-NaOH (pH 7.5), 1 M NaCl, 5% (v/v) glycerol, 1% (v/v) Tween 20, and 10 mM imidazole] and eluted with buffer A using a linear gradient of 20 to 300 mM imidazole over 47 ml. Fractions corresponding to AtRLPH2-V5-H6 were pooled and subjected to spin dialysis using a 30-kDa MWCO concentrator (Millipore). Concentrated protein was diluted in 10 ml of buffer B [25 mM MES (pH 6.0), 5% (v/v) glycerol] and loaded onto a 1-ml HiTrap SP column (GE Healthcare) before elution with buffer B using a linear gradient of 0 to 0.6 M NaCl over 13 ml. After spin dialysis into 100 mM Mops-NaOH (pH 7.5), 150 mM NaCl, and 5% (v/v) glycerol, protein was concentrated to 4.7 mg/ml [extinction coefficient at 280 nm calculated by ExPASy ProtParam web server (https://web.expasy.org/peptide_mass/)], flash-frozen in liquid nitrogen, and stored at −80°C.

Protein crystallization

AtRLPH2-V5-H6 was crystallized by hanging-drop vapor diffusion. AtRLPH2-V5-H6 (2 µl × 4.7 mg/ml) was mixed with a solution of 100 mM bis-tris-Cl (pH ~6) and polyethylene glycol 3350 (250 g/liter) and glycerol (200 g/liter). Needle-shaped crystals appeared overnight, and crystals were allowed to grow for 14 to 21 days at room temperature before flash-cooling in liquid nitrogen. Isomorphous crystals were also grown in the presence of 1 mM sodium tungstate under conditions similar to the native crystals.

Data collection, structure determination, and refinement

A single crystal was suspended in a microfabricated loop (MicroLoop E, 0.5 mm × 0.05 mm, MiTeGen) and flash-cooled in liquid nitrogen. The crystal was shipped to the Stanford Synchrotron Radiation Laboratory Beamline 12-2. Data were measured from a single needle-like crystal (1.0 mm × 0.01 mm × 0.01 mm) using a microfocus beam (20 × 20 µm, 6690 eV, 1.853 Å). Diffraction images were measured in shutterless mode using a Dectris Pilatus 6M pixel array detector (0.5°, 1 s, 500 images) at a distance of 188.1 mm. The crystal was translated every 50 images to reduce the effects of radiation decay. XDS was used to index, integrate, and scale the diffraction data (*30*). Phenix was used to determine and refine the positions of the anomalous scattering atoms, to calculate phases and electron density maps, and to build an initial model comprising 208 of 309 residues (*31*). Nearly all of the remaining residues in the protein were modeled manually during the refinement process, apart from three residues at the N terminus and residues 140 to 147, which are not clearly defined by electron density maps and appear to be disordered. COOT (*32*) was used for model building and visualization of electron density maps, and REFMAC was used for refinement. Data were also measured for an isomorphous native crystal diffracting to higher resolution, measured at the Canadian Light Source Beamline 08B1-1 (200-µm beam, 12,658 eV, 0.979 Å). Data were also measured for an isomorphous crystal cocrystallized with 1 mM sodium tungstate, also measured at Beamline 08B1-1 (200-µm beam, 10,212 eV, 1.214 Å). The structure of the ERK1/2 peptide substrate (HTGFLpTEpYVATR) was modeled by assuming backbone torsion angles characteristic of an antiparallel beta conformation and common rotamers for side chains that did not clash with the peptide-binding groove of AtRLPH2. The locations of the two phosphoryl groups in the phosphothreonine and phosphotyrosine residues were anchored at positions that coincide with the experimentally determined locations of the tungstate ions observed in the structure of AtRLPH2 cocrystallized with sodium tungstate. The structure of the complex was refined with 100 steps of steepest descent minimization and 10 steps of conjugate gradient minimization using the MMTK routines in UCSF Chimera v. 1.11.2.

Bioinformatics

AtRLPH2 (accession AEE74842.1) and RLPH2 homolog sequences were retrieved from Uhrig *et al.* (*8*) or by using AtRLPH2 and DELTA-BLAST at the National Center for Biotechnology Information (NCBI). Sequences were aligned in Clustal Omega (http://www.clustal.org/), visualized, and hand-edited in GeneDoc (http://genedoc.software.informer.com/2.7/). The *A. thaliana* PPP-family sequences for PP1 (TOPP1 to TOPP9), PP2A-C1 to PP2A-C5, PP4-C1 and PP4-C2, and PP6-C1 and PP6-C3 were obtained from NCBI and aligned as above for RLPH2 sequences. All protein and organism names and accession numbers for proteins used in alignments (figs. S1 and S2) are shown in table S1.

Malachite green dephosphorylation assays

Purified AtRLPH2-V5-H6 (1 µg) was incubated for 30 min at 30°C in 160 µl of assay buffer [100 mM Hepes-NaOH (pH 7.5), 150 mM NaCl] containing varying amounts of ERK1/2 peptides (HTGFLTEYVATR) (Fig. 4) or 0.25 mM ERK1/2 peptides (fig. S3), either single- or dual-phosphorylated on the TEY motif. Control assays were performed without enzyme. The reaction was stopped with 40 µl of malachite green solution and measured at 630 nm on a Molecular Devices SpectraMax Plus 384 UV/Vis microplate reader. Activity was calculated by Pi release determined by a standard curve measured in parallel (*5*). Assays were done three times in triplicate and are presented as mean ± SEM. V_{max} and K_m were calculated using SciDAVis (http://scidavis.sourceforge.net/), using nonlinear least squares curve fitting functions to fit the data.

On-blot dephosphorylation assays and immunoblotting

ERK1/2 phosphopeptides were covalently linked to BSA as in the study of Uhrig *et al.* (*10*) and spotted onto a nitrocellulose membrane, which was then blocked and incubated with AtRLPH2-V5-H6 (1.5 µg/ml) in 1% (w/v) BSA for 1 hour at room temperature. A control experiment was performed in parallel with BSA only. Membranes were probed with either antibody recognizing pTyr (1:500; Santa Cruz Biotechnology) or pThr antibody (1:2000; Cell Signaling Technology) in the presence of phosphatase inhibitors (25 mM NaF and 1 mM Na_3VO_4) followed by horseradish peroxidase–labeled goat anti-mouse secondary antibody (PerkinElmer) and development with enhanced chemiluminescence substrate (ECL, PerkinElmer). All blots were performed three times in parallel and developed at the same time, and one representative blot is shown.

Site-directed mutagenesis

R51A, R245A, R132S, and K238S single mutants and R132S, K238S double mutants were generated using the QuikChange Lightning Multi Site-Directed Mutagenesis Kit (Agilent). Primers used are shown in table S2. Mutants were sequenced to confirm changes. Mutated proteins were expressed and purified as described for the wild-type enzyme.

SUPPLEMENTARY MATERIALS

www.sciencesignaling.org/cgi/content/full/11/524/eaan8804/DC1

Fig. S1. Multiple sequence alignment of AtRLPH2 with other RLPH2 class members.

Fig. S2. Multiple sequence alignment of AtRLPH2 with other PPP family members from *A. thaliana*.

Fig. S3. Enzymatic activity of RLPH2 mutated in phosphothreonine-binding and gatekeeper residues.

Fig. S4. Different rotamers may be adopted by phosphothreonine in the pTEpY peptide substrate versus threonine in the TEpY peptide substrate.
Fig. S5. Location of motif 1 in RLPH2.
Table S1. Accession numbers of proteins used for sequence alignments.
Table S2. Primers used to create the AtRLPH2-V5-H6 mutants.
Movie S1. AtRLPH2 substrate-binding groove.

REFERENCES AND NOTES

1. T. Hunter, T. Pawson, The evolution of protein phosphorylation. Preface. *Philos. Trans. R. Soc. Lond. B Biol. Sci.* **367**, 2512 (2012).
2. K. Sharma, R. C. J. D'Souza, S. Tyanova, C. Schaab, J. R. Wiśniewski, J. Cox, M. Mann, Ultradeep human phosphoproteome reveals a distinct regulatory nature of Tyr and Ser/Thr-based signaling. *Cell Rep.* **8**, 1583–1594 (2014).
3. N. K. Tonks, Protein tyrosine phosphatases—From housekeeping enzymes to master regulators of signal transduction. *FEBS J.* **280**, 346–378 (2013).
4. G. B. G. Moorhead, V. De Wever, G. Templeton, D. Kerk, Evolution of protein phosphatases in plants and animals. *Biochem. J.* **417**, 401–409 (2009).
5. D. M. Silver, L. P. Silva, E. Issakidis-Bourguet, M. A. Glaring, D. C. Schriemer, G. B. G. Moorhead, Insight into the redox regulation of the phosphoglucan phosphatase SEX4 involved in starch degradation. *FEBS J.* **280**, 538–548 (2013).
6. D. Kerk, G. Templeton, G. B. G. Moorhead, Evolutionary radiation pattern of novel protein phosphatases revealed by analysis of protein data from the completely sequenced genomes of humans, green algae, and higher plants. *Plant Physiol.* **146**, 351–367 (2008).
7. A. Shankar, N. Agrawal, M. Sharma, A. Pandey, K. P. M. Girdhar, Role of protein tyrosine phosphatases in plants. *Curr. Genomics* **16**, 224–236 (2015).
8. R. G. Uhrig, D. Kerk, G. B. Moorhead, Evolution of bacteria-like phosphoprotein phosphatases in photosynthetic eukaryotes features ancestral mitochondrial or archaeal origin and possible lateral gene transfer. *Plant Physiol.* **163**, 1829–1843 (2013).
9. A. V. Andreeva, M. A. Kutuzov, Widespread presence of "bacterial-like" PPP phosphatases in eukaryotes. *BMC Evol. Biol.* **4**, 47 (2004).
10. R. G. Uhrig, A.-M. Labandera, J. Muhammad, M. Samuel, G. B. Moorhead, Rhizobiales-like phosphatase 2 from *Arabidopsis thaliana* is a novel phospho-tyrosine-specific phospho-protein phosphatase (PPP) family protein phosphatase. *J. Biol. Chem.* **291**, 5926–5934 (2016).
11. Y. Shi, Serine/threonine phosphatases: Mechanism through structure. *Cell* **139**, 468–484 (2009).
12. H. Tsuruta, B. Mikami, Y. Aizono, Crystal structure of cold-active protein-tyrosine phosphatase from a psychrophile, *Shewanella* sp. *J. Biochem.* **137**, 69–77 (2005).
13. Q.-H. Wang, W.-X. Hu, W. Gao, R.-C. Bi, Crystal structure of the diadenosine tetraphosphate hydrolase from *Shigella flexneri* 2a. *Proteins* **65**, 1032–1035 (2006).
14. W. C. Voegtli, D. J. White, N. J. Reiter, F. Rusnak, A. C. Rosenzweig, Structure of the bacteriophage λ Ser/Thr protein phosphatase with sulfate ion bound in two coordination modes. *Biochemistry* **39**, 15365–15374 (2000).
15. L. K. Wang, U. Das, P. Smith, S. Shuman, Structure and mechanism of the polynucleotide kinase component of the bacterial Pnkp-Hen1 RNA repair system. *RNA* **18**, 2277–2286 (2012).
16. L. Holm, P. Rosenström, Dali server: Conservation mapping in 3D. *Nucleic Acids Res.* **38**, W545–W549 (2010).
17. M.-P. Egloff, P. T. W. Cohen, P. Reinemer, D. Barford, Crystal structure of the catalytic subunit of human protein phosphatase 1 and its complex with tungstate. *J. Mol. Biol.* **254**, 942–959 (1995).
18. M. Terrak, F. Kerff, K. Langsetmo, T. Tao, R. Dominguez, Structural basis of protein phosphatase 1 regulation. *Nature* **429**, 780–784 (2004).
19. M. J. Ragusa, B. Dancheck, D. A. Critton, A. C. Nairn, R. Page, W. Peti, Spinophilin directs protein phosphatase 1 specificity by blocking substrate binding sites. *Nat. Struct. Mol. Biol.* **17**, 459–464 (2010).
20. Y. Xu, Y. Xing, Y. Chen, Y. Chao, Z. Lin, E. Fan, J. W. Yu, S. Strack, P. D. Jeffrey, Y. Shi, Structure of the protein phosphatase 2A holoenzyme. *Cell* **127**, 1239–1251 (2006).
21. Y. Xu, Y. Chen, P. Zhang, P. D. Jeffrey, Y. Shi, Structure of a protein phosphatase 2A holoenzyme: Insights into B55-mediated Tau dephosphorylation. *Mol. Cell* **31**, 873–885 (2008).
22. D. R. Davies, W. G. J. Hol, The power of vanadate in crystallographic investigations of phosphoryl transfer enzymes. *FEBS Lett.* **577**, 315–321 (2004).
23. H. Nakagami, N. Sugiyama, K. Mochida, A. Daudi, Y. Yoshida, T. Toyoda, M. Tomita, Y. Ishihama, K. Shirasu, Large-scale comparative phosphoproteomics identifies conserved phosphorylation sites in plants. *Plant Physiol.* **153**, 1161–1174 (2010).
24. N. Sugiyama, H. Nakagami, K. Mochida, A. Daudi, M. Tomita, K. Shirasu, Y. Ishihama, Large-scale phosphorylation mapping reveals the extent of tyrosine phosphorylation in *Arabidopsis*. *Mol. Syst. Biol.* **4**, 193 (2008).
25. B. Wang, X. Qin, J. Wu, H. Deng, Y. Li, H. Yang, Z. Chen, G. Liu, D. Ren, Analysis of crystal structure of *Arabidopsis* MPK6 and generation of its mutants with higher activity. *Sci. Rep.* **6**, 25646 (2016).
26. W. Peti, A. C. Nairn, R. Page, Structural basis for protein phosphatase 1 regulation and specificity. *FEBS J.* **280**, 596–611 (2013).
27. H. Tsuruta, Y. Aizono, Enzymatical properties of psychrophilic phosphatase I. *J. Biochem.* **125**, 690–695 (1999).
28. A. Peck, F. Sunden, L. D. Andrews, V. S. Pande, D. Herschlag, Tungstate as a transition state analog for catalysis by alkaline phosphatase. *J. Mol. Biol.* **428**, 2758–2768 (2016).
29. C. J. Caunt, S. M. Keyse, Dual-specificity MAP kinase phosphatases (MKPs): Shaping the outcome of MAP kinase signalling. *FEBS J.* **280**, 489–504 (2013).
30. W. Kabsch, Automatic indexing of rotation diffraction data from crystals of initially unknown symmetry and cell constants. *J. Appl. Cryst.* **26**, 795–800 (1993).
31. P. D. Adams, P. V. Afonine, G. Bunkóczi, V. B. Chen, I. W. Davis, N. Echols, J. J. Headd, L.-W. Hung, G. J. Kapral, R. W. Grosse-Kunstleve, A. J. McCoy, N. W. Moriarty, R. Oeffner, R. J. Read, D. C. Richardson, J. S. Richardson, T. C. Terwilliger, P. H. Zwart, PHENIX: A comprehensive Python-based system for macromolecular structure solution. *Acta Crystallogr. D Biol. Crystallogr.* **66**, 213–221 (2010).
32. P. Emsley, K. Cowtan, *Coot*: Model-building tools for molecular graphics. *Acta Crystallogr. D Biol. Crystallogr.* **60**, 2126–2132 (2004).
33. P. A. Karplus, K. Diederichs, Linking crystallographic model and data quality. *Science* **336**, 1030–1033 (2012).
34. V. B. Chen, W. B. Arendall III, J. J. Headd, D. A. Keedy, R. M. Immormino, G. J. Kapral, L. W. Murray, J. S. Richardson, D. C. Richardson, *MolProbity*: All-atom structure validation for macromolecular crystallography. *Acta Crystallogr. D Biol. Crystallogr.* **66**, 12–21 (2010).

Acknowledgments: We thank D. Alessi of the Medical Research Council Protein Phosphorylation and Ubiquitylation Unit (University of Dundee) for several phosphopeptides used in assays and L. Eugenio for assistance with crystallization screening. **Funding:** Funding for this work was provided by the Natural Sciences and Engineering Research Council of Canada (G.B.M. and K.K.S.N.) and Alberta Innovates Technology Futures and University of Calgary Silver Anniversary Graduate Fellowship (A.-M.L.). **Author contributions:** R.G.U. cloned AtRLPH2 and, with K.C., purified the enzyme and performed initial crystallization work. A.-M.L. performed further crystallization optimization and all other biochemistry. K.K.S.N. did the structure determination and structure analysis. G.B.M., A.-M.L., and K.K.S.N. wrote the manuscript. **Competing interests:** The authors declare that they have no competing financial interests. **Data and materials availability:** The atomic coordinates and experimental data for the uncomplexed and tungstate-complexed structures of AtRLPH2 have been deposited in the Research Collaboratory for Structural Bioinformatics Protein Data Bank (PDB), PDB ID codes 5VJV and 5VJW, respectively.

Submitted 1 June 2017
Accepted 9 March 2018
Published 3 April 2018
10.1126/scisignal.aan8804

Citation: A.-M. Labandera, R. G. Uhrig, K. Colville, G. B. Moorhead, K. K. S. Ng, Structural basis for the preference of the *Arabidopsis thaliana* phosphatase RLPH2 for tyrosine-phosphorylated substrates. *Sci. Signal.* **11**, eaan8804 (2018).

Science Signaling

Structural basis for the preference of the *Arabidopsis thaliana* phosphatase RLPH2 for tyrosine-phosphorylated substrates

Anne-Marie Labandera, R. Glen Uhrig, Keaton Colville, Greg B. Moorhead and Kenneth K. S. Ng

Sci. Signal. **11** (524), eaan8804.
DOI: 10.1126/scisignal.aan8804

Substrate specificity of an unusual phosphatase

The plant phosphatase RLPH2 is a member of the phosphoserine- and phosphothreonine-specific protein phosphatase (PPP) family; however, it prefers substrates that contain phosphotyrosine residues to those that contain phosphoserine or phosphothreonine residues. Labandera *et al*. solved crystal structures of RLPH2 both in its native form and in complex with the phosphate mimic tungstate and performed biochemical assays with various mutant forms of RLPH2. These approaches revealed the structural basis for the preference of RLPH2 for phosphotyrosine, particularly substrates that are dually phosphorylated on both tyrosine and a nearby threonine residue. These findings explain the unusual properties of this phosphatase, and the preference for substrates containing a pTxpY motif suggests that mitogen-activated protein kinases (MAPKs) may be substrates for RLPH2 in vivo.